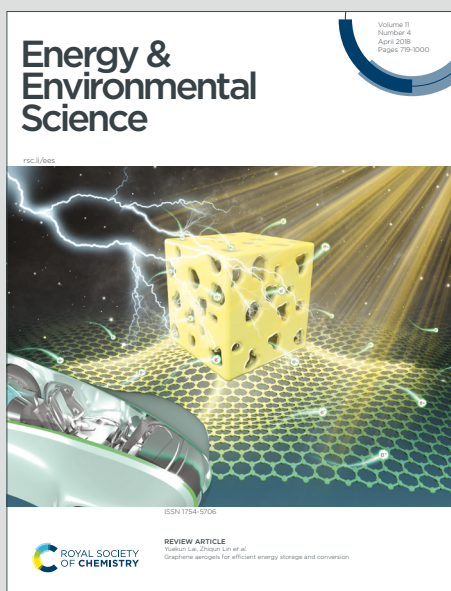


# Energy & Environmental Science

Accepted Manuscript

This article can be cited before page numbers have been issued, to do this please use: K. Kim, B. Koo, Y. Jo, S. Lee, J. K. Kim, B. Kim, W. Jung and J. W. Han, *Energy Environ. Sci.*, 2020, DOI: 10.1039/D0EE01308K.



This is an Accepted Manuscript, which has been through the Royal Society of Chemistry peer review process and has been accepted for publication.

Accepted Manuscripts are published online shortly after acceptance, before technical editing, formatting and proof reading. Using this free service, authors can make their results available to the community, in citable form, before we publish the edited article. We will replace this Accepted Manuscript with the edited and formatted Advance Article as soon as it is available.

You can find more information about Accepted Manuscripts in the [Information for Authors](#).

Please note that technical editing may introduce minor changes to the text and/or graphics, which may alter content. The journal's standard [Terms & Conditions](#) and the [Ethical guidelines](#) still apply. In no event shall the Royal Society of Chemistry be held responsible for any errors or omissions in this Accepted Manuscript or any consequences arising from the use of any information it contains.

### Broader context

Till now, ex-solution has been actively applied to synthesize highly active and durable catalysts. However, the lack of a fundamental understanding of the atomic-level origin of the phenomena was a main hurdle to practically apply it to further improve the activity and stability of catalytic materials. To tackle this issue, we systematically performed density functional theory calculations to identify the driving force of Co ex-solution from  $\text{Sr}(\text{Ti}, \text{Co})\text{O}_3$  with experimental verifications. As a result, we found that the Co vacancy formation energy is a key driving force of Co ex-solution, and the degree of Co vacancy formation is originated from the cation-oxygen bond strength, which can be represented by the Co-O bond length at the atomic scale. In this aspect, this work comprehensively broadened our understanding for the driving force of B-metal ex-solution in perovskite materials, and suggested a way to effectively control the ex-solution. These findings can be practically applied to improve catalytic activity and durability in various catalytic applications.

# Control of transition metal - oxygen bond strength boosts the redox ex-solution in perovskite oxide surface

Kyeounghak Kim<sup>a,†</sup>, Bonjae Koo<sup>b,†</sup>, Yong-Ryun Jo<sup>c</sup>, Siwon Lee<sup>b</sup>, Jun Kyu Kim<sup>b</sup>, Bong-Joong Kim<sup>c,\*</sup>, WooChul Jung<sup>b,\*</sup>, and Jeong Woo Han<sup>a,\*</sup>

<sup>a</sup>*Department of Chemical Engineering, Pohang University Science and Technology (POSTECH), Pohang, Gyeongbuk 37673, Republic of Korea*

<sup>b</sup>*Department of Materials Science and Engineering, Korea Advanced Institute of Science and Technology (KAIST), Daejeon 34141, Republic of Korea*

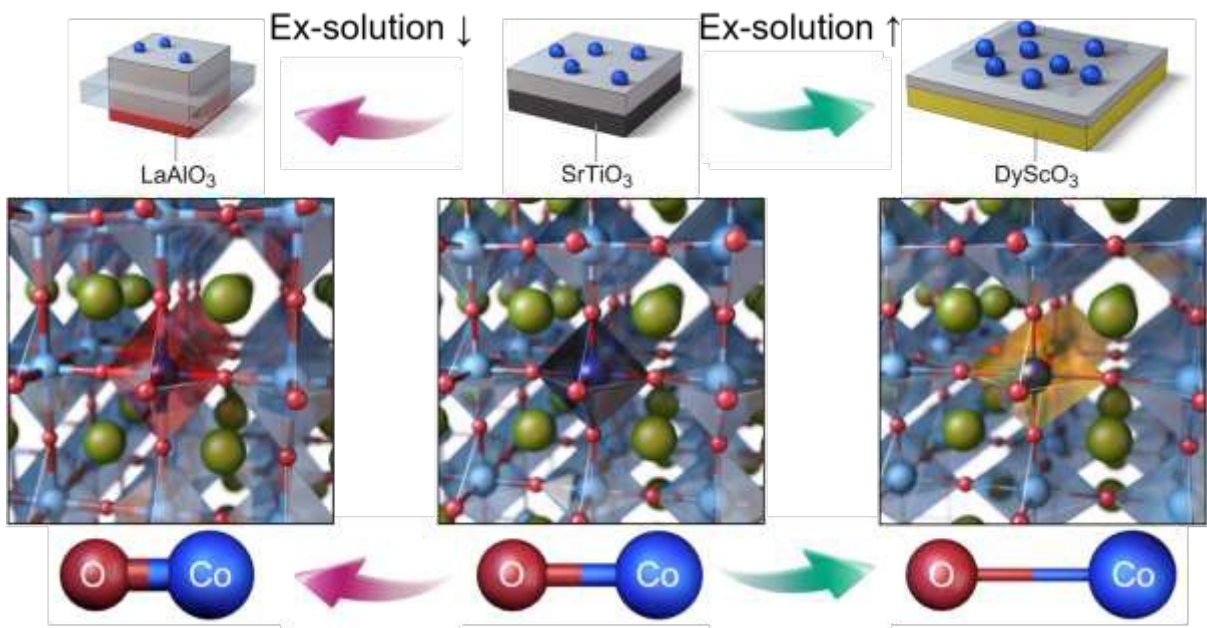
<sup>c</sup>*School of Materials Science and Engineering, Gwangju Institute of Science and Technology (GIST), Gwangju 61005, Republic of Korea*

## Abstract

We demonstrate theoretically and experimentally that engineering of cation-oxygen bond strength in perovskite structure can control redox ex-solution of B-site metal and thus the formation of metal nanoparticles at the oxide surface upon high-temperature reduction. Especially, we show that large isovalent doping significantly promotes the B-site ex-solution by tuning of the cation-oxygen bond strength, leading to the high catalytic activity of CO oxidation. This method to promote ex-solution can be readily applied to various heterogeneous catalysts.

\*Corresponding authors: [jwhan@postech.ac.kr](mailto:jwhan@postech.ac.kr), [wjchung@kaist.ac.kr](mailto:wjchung@kaist.ac.kr), [kimbj@gist.ac.kr](mailto:kimbj@gist.ac.kr)

Table of contents (TOC)



Tuning of cation-oxygen bond strength effectively promotes B-site ex-solution in a perovskite, thereby boosting the catalytic activity of CO oxidation.

## Introduction

Metal nanoparticles (NPs) have high surface-to-volume ratios and possibly unique catalytic properties. In particular, when the particles are dispersed on oxide supports, their utilization is increased and the catalytic ability of NPs is often greatly improved compared to that of pure metal NPs<sup>1-8</sup>. Therefore, they are widely used as heterogeneous catalysts for various reactions. However, small metal particles are unavoidably sintered at high temperatures ( $> 500\text{ }^{\circ}\text{C}$ ), and this process severely decreases their catalytic activity<sup>9-12</sup>. Moreover, current methods to synthesize monodispersed metal NPs and evenly disperse them on the oxide support surface are tedious and costly<sup>1-8,11,13,14</sup>.

‘Ex-solution’ is *in situ* growth of metal NPs directly from oxide support. The phenomenon has been exploited in the fields of high-temperature catalysis and renewable energy<sup>15-27</sup>. When perovskite oxides ( $\text{ABO}_3$ , where A and B represent cations) are used as a hosting framework, cations of transition metal can dissolve in the B-sites of the perovskite lattice under oxidizing conditions; upon subsequent reduction the metals ex-solve as nanometer-sized metallic phases on the oxide surface. This process is faster, less expensive, and allows finer and better particle distribution than traditional techniques to synthesize and disperse NPs. Moreover, it is reversible, so that catalyst agglomeration can be avoided by exploiting re-oxidation, and thereby significantly extending the lifetime of the supported catalysts<sup>28,29</sup>.

The mechanism that drives ex-solution is not completely understood<sup>15,16,19,21,30-34</sup>. The key to this phenomenon is the stability of certain cations in a perovskite lattice, so the bond strength (or length) between cations and neighboring oxygen anions may determine the outcome of ex-solution. However, to the best of our knowledge, no study has considered the atom-level stability of a reducible cation surrounded by six oxygen ions in a lattice, even

though understanding of this characteristic might guide development of a method to effectively control the amount or distribution of the ex-solved particles.

Here, we quantify how the ex-solution of a B-site transition metal is affected by the bond strength between it and its neighbor oxygen ions in a perovskite lattice. We first simulated how deformation of the perovskite lattice affects the cation-oxygen bond strength and thus affects the stability of individual elements. Taking Co-doped SrTiO<sub>3</sub> (SrTi<sub>0.75</sub>Co<sub>0.25</sub>O<sub>3</sub>, STC) as a model system, we calculated the vacancy formation energies of all constituent atoms as a function of lattice strain. We found that neither the Sr-O, the Ti-O, nor the Co-O bonds are in their most stable states individually, but that they are in an optimal balance at zero strain, thereby stabilizing the overall perovskite. This balance suggests that local instability of Co-O bonds may drive Co ex-solution from the STC lattice. To test this hypothesis, we fabricated highly-strained epitaxial thin films of STC and monitored how the lattice strain affects the surface composition and CO oxidation reactivity. Extending these observations, we further demonstrated that the Co-O bond strength can be sufficiently weakened by introducing a large isovalent dopant (in this case, Ba) in the A-site of the perovskite lattice, and thereby offer a new strategy to activate the ex-solution phenomenon.

## Result & Discussion

As an indicator of the stability of a cation in perovskite lattice, the bond length may predict the bond strength with the surrounding oxygen atoms<sup>35</sup>. Our previous work successfully explained that Sr enrichment in SrTi<sub>0.5</sub>Fe<sub>0.5</sub>O<sub>3-δ</sub> (STF) can be suppressed under tensile strain, because Sr cations are not intrinsically in the most stable state in the equilibrium SrTiO<sub>3</sub> (STO) lattice; therefore, using tensile strain to increase the Sr-O bond length up to certain range can stabilize the Sr cations<sup>35</sup>. In contrast, tensile strain destabilizes the B-metal atom (Ti in STO); this trend suggests that segregation of B-metal might be

facilitated by increasing the Ti-O bond length. Therefore, here we investigate whether this possible effect is also effective to control Co ex-solution from STC. To control the Co-O bond length, we applied biaxial strain to STC by growing it epitaxially on single-crystal substrates that have different lattice parameters.

To implement this experimental condition in our density functional theory (DFT) calculation, we optimized the bulk STC under biaxial strain. The Co cation binds with surrounding oxygen atoms by four in-plane bonds (Bond A) and two out-of-plane bonds (Bond B) (Fig. S1a). Tensile strain increases the lengths of the in-plane Co-O bonds and simultaneously decreases the lengths of the out-of-plane Co-O bonds to maintain the Poisson ratio of the crystal structure, and the average length of Co-O bonds (and thus unit cell volume) increases (Fig. 1a and Table S1), so their average strengths weaken. This change results in a decrease in Co segregation energy  $E_{\text{Co,seg}}$  as the applied tensile strain increases (Fig. 1b).

To explore the energy requirement for the segregation of Co towards the top layer of STC surface, and thus describe Co ex-solution tendency (Fig. S2), we calculated  $E_{\text{Co,seg}}$  as a function of biaxial strain. Co segregated preferentially towards the surface as the applied tensile increased (Fig. 1b) and the Co-O bond length was increasingly stretched (Fig. 1a). The stability of Co declined as Co-O bond length increased, so the ex-solution of Co was facilitated. This implies that the engineering of cation stability for Co ex-solution by controlling Co-O bond strength in a parental perovskite lattice can also be effective in STC. In the view of defect chemistry, the Co ex-solution on the STC surface can be described by the combination of partial Schottky defect formation and reduction. According to the previous report<sup>36</sup>, the relation between the enthalpies of Co ex-solution and  $E_{\text{Co,vac}}$  is finally derived to be linearly proportional to each other.

For Sr and Ti, the formation energies  $E_{\text{Sr,vac}}$  for Sr vacancies and  $E_{\text{Ti,vac}}$  for Ti vacancies showed quite similar curve shapes to those in our previous model structure<sup>35</sup> (Fig. 1c). As the tensile strain was increased,  $E_{\text{Sr,vac}}$  continuously increased, whereas  $E_{\text{Co,vac}}$  continuously decreased. All such *general* vacancy formation energies  $E_{\text{X,vac}}$  are parabolic curves<sup>35,37</sup>; this trend implies the existence of an optimal bond length that yields the highest stability between cation and lattice oxygen in perovskite (Fig. 1d).  $E_{\text{Co,vac}}$  steadily increased as the bond length of Co-O decreased, so an optimal point for Co stability might exist below the mechanical strain region of  $-3\%$ . The optimal strain for cation stability is positive for the A-site (Sr), but negative for the B-site (Co or Ti). Thus, under tensile strain, the stability of A-site cation preferentially increased whereas that of B-site cation decreased, allowing us to selectively weaken the stability of B-site cation under tensile strain. In particular,  $E_{\text{Co,vac}}$  is significantly lower than that of  $E_{\text{Sr,vac}}$  or  $E_{\text{Ti,vac}}$  over the strain ranges, so Co would respond the most sensitively to the structural deformation of perovskite, enabling the acceleration of Co exsolution by applying tensile strain to STC (Fig. 1b). In addition, surface oxygen vacancy formation energy, which represents the reducibility of segregated cation to the metallic phase, decreased under tensile strain. Therefore, the increase of Co-O bond length also facilitates the reduction of segregated Co to form metallic nanoparticles over the STC surface (Fig. S3).



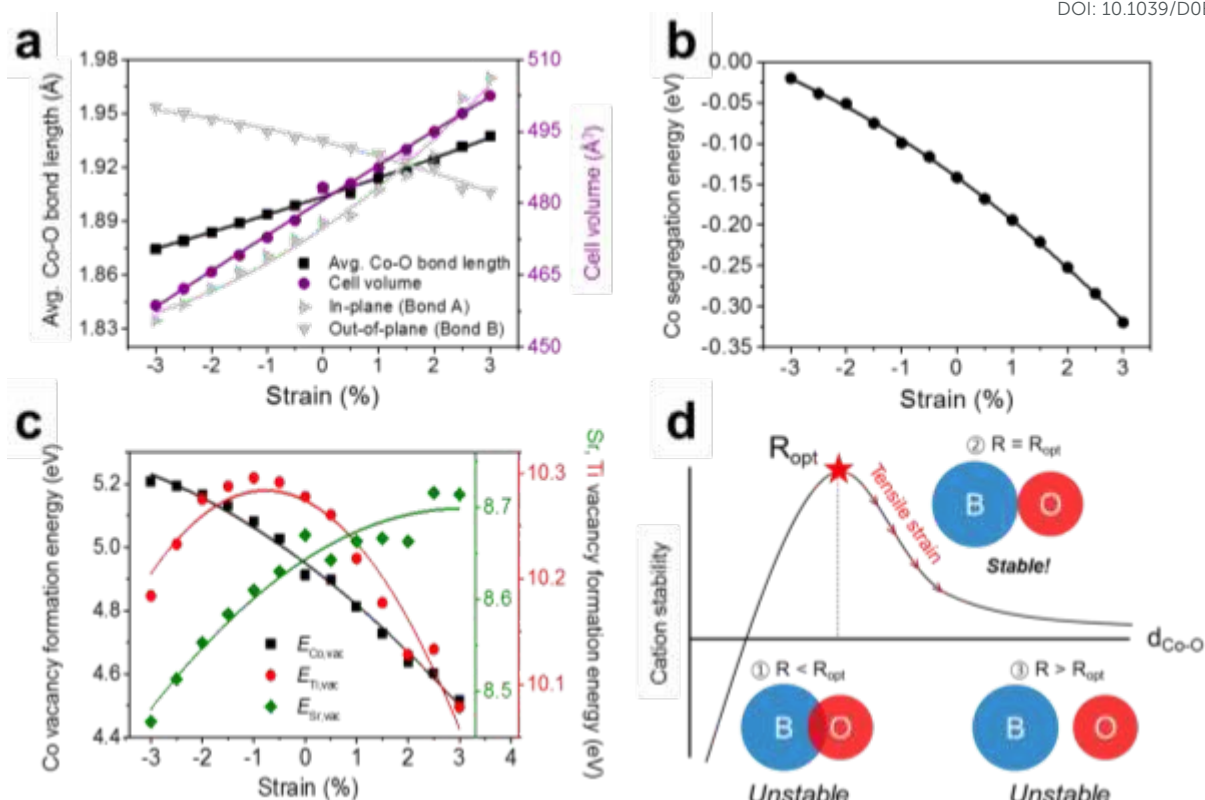


**Figure 1.** (a) DFT-calculated in-plane, out-of-plane, and average Co-O bond length and the cell volume of STC as a function of biaxial strain. (b) Co segregation energy ( $E_{\text{Co,seg}}$ ) towards the surface on a slab model of STC under biaxial strain. (c) Vacancy formation energies of Co, Sr, and Ti ( $E_{\text{Co,vac}}$ ,  $E_{\text{Sr,vac}}$ ,  $E_{\text{Ti,vac}}$ ) in bulk SrTi<sub>0.75</sub>Co<sub>0.25</sub>O<sub>3</sub> (STC) under biaxial strain. (d) Schematic illustration of B-site cation stability according to bond length of Co-O.

To experimentally demonstrate the effects of bond strength on the degree of Co exsolution, we used pulsed laser deposition (PLD) to fabricate strain-controlled STC thin films by lattice mismatch with single-crystal substrates of LaAlO<sub>3</sub>(001) (LAO), SrTiO<sub>3</sub>(001) (STO) and DyScO<sub>3</sub>(110) (DSO). After deposition, samples were heat-treated in a chamber at 700 °C in ultra-high vacuum for 1 h: the condition was reductive enough for Co to be ex-solved, but not enough for the lattice strain of each film to be relaxed completely.

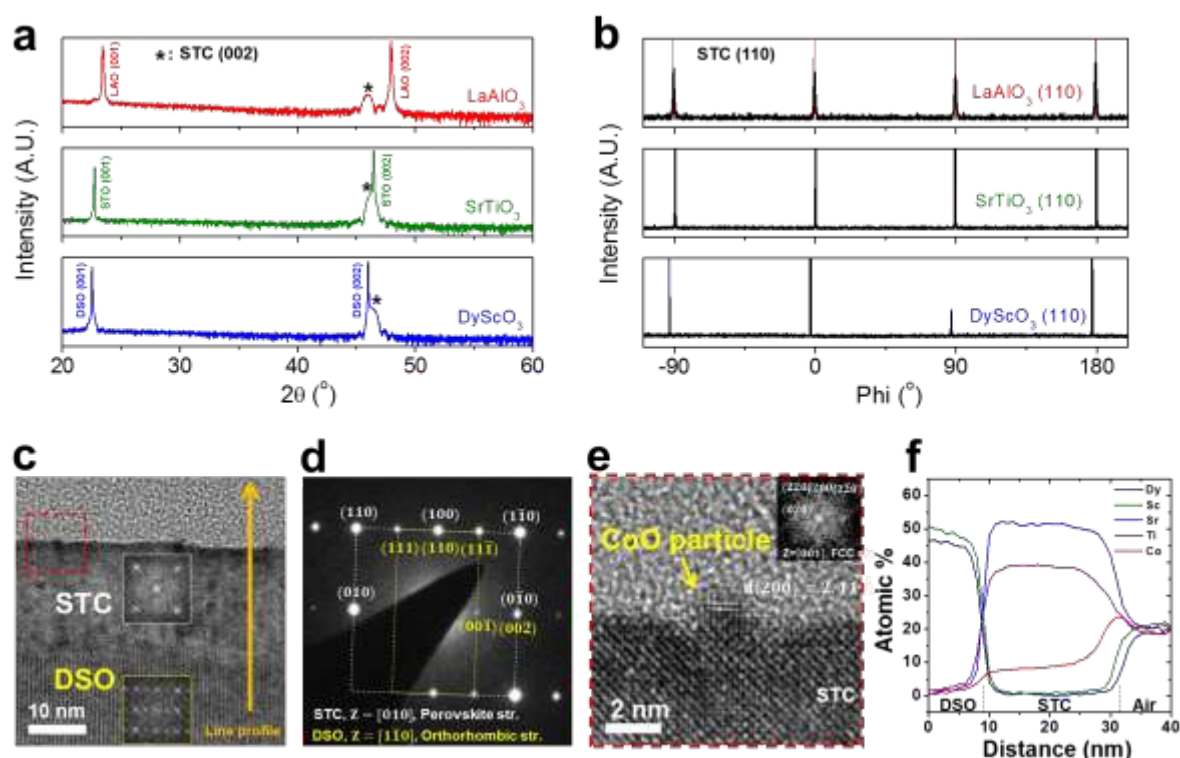


**Figure 2.** (a) Out-of-plane diffraction patterns ( $2\theta$ - $\omega$  scan) of (001)-oriented epitaxial  $\text{SrTi}_{0.75}\text{Co}_{0.25}\text{O}_{3-\delta}$  (STC) thin films on (001)-oriented  $\text{LaAlO}_3$  (LAO),  $\text{SrTiO}_3$  (STO) and (110)-oriented  $\text{DyScO}_3$  (DSO) single-crystal substrates. (b) In-plane diffraction patterns ( $\Phi$  scan) of the (001)-oriented epitaxial STC thin films on LAO, STO and DSO substrates. Each  $\Phi$  scan was collected for the (110) peak after tilting the sample by  $45^\circ$ . (c) Cross-sectional high-resolution transmission electron microscope (HR-TEM) image and the fast Fourier transform (FFT) patterns corresponding to the layers of STC (inset in white box) and DSO (inset in yellow box). (d) Selected area electron diffraction (SAED) pattern of the areas in taken at  $[010]_{\text{STC}}$  and  $[1\bar{1}0]_{\text{DSO}}$  zone axis. (e) Magnified HR-TEM image and the FFT patterns of the STC surface on a single-crystal DSO substrate (the area marked by the red-dotted box in (c)). The FFT pattern (inset) was obtained from a single CoO particle taken from the  $[001]_{\text{CoO}}$  zone axis. (f) Energy dispersive X-ray spectroscopy (EDS) line scan data of the region indicated by the arrow in (c).

High-resolution X-ray diffraction (HR-XRD) out-of-plane diffraction patterns ( $2\theta$ - $\omega$  scan) (Fig. 2a) were obtained for each film. The in-plane patterns ( $\Phi$  scan) exhibited  $90^\circ$  rotational symmetry of the crystallographic plane normal to the incident beam; this result confirms

good alignment registry between the film and substrate (Fig. 2b). Both in-plane and out-of-plane strain were calculated by the values of the relaxed lattice parameter  $\hat{a}$  of each film with applying a Poisson ratio of 0.232 ( $\text{SrTiO}_3$ )<sup>38,39</sup>. The in-plane strain state  $\epsilon_{xx}$  of STC thin films on LAO and STO substrates were compressed by 1.97% and 0.66%, respectively, whereas the stretched film on DSO showed tensile strain of +0.14% along the in-plane direction (Table 1). The increase of Co-O bond length was also confirmed as more tensile strain applied to STC thin films (Table S2).

**Table 1.** Calculated misfit strain of  $\text{SrTi}_{0.75}\text{Co}_{0.25}\text{O}_{3-\delta}$  (STC) thin films. The strained and relaxed lattice parameters of epitaxial STC thin films were collected from the HR-XRD data. The strained in-plane and out-of-plane lattice parameters of STC films were calculated by combining the interplanar distance of the (002) and (110) peaks.

Substrate	Constrained in-plane lattice parameter $a$ [Å]	Constrained out-of-plane lattice parameter $c$ [Å]	Relaxed film lattice parameter $\hat{a}$ [Å]	In-plane strain [%] $\epsilon_{xx} = 100 \frac{(a - \hat{a})}{\hat{a}}$	Out-of-plane strain [%] $\epsilon_{zz} = 100 \frac{(c - \hat{a})}{\hat{a}}$
$\text{LaAlO}_3$ (3.790 Å)	3.812	3.935	3.889	-1.97	1.19
$\text{SrTiO}_3$ (3.905 Å)	3.858	3.932	3.917	-0.66	0.40
$\text{DyScO}_3$ (3.948 Å)	3.922	3.913	3.916	0.14	-0.09

\*  $\hat{a}$  was calculated from  $\frac{\Delta c}{c} = \frac{-2\nu \Delta a}{1-\nu \hat{a}}$ , assuming  $\hat{a} = \hat{c}$  and  $\nu = 0.232$  for STC<sup>39</sup>

A cross-sectional high-resolution transmission electron microscopy (HR-TEM) image and the fast Fourier transformation (FFT) patterns of the STC and DSO layers revealed that the STC thin film is a single crystal with a perovskite structure and a thickness of ~25 nm (Fig. 2c). The selected area electron diffraction (SAED) pattern (Fig. 2d) of the area in Fig. 2c shows that (100)<sub>STC</sub> is coincident with (110)<sub>DSO</sub>, and that (0-10)<sub>STC</sub> is coincident with (00-2)<sub>DSO</sub>. These results indicate that the STC layer is epitaxially grown with identical lattice spacings in the two orthogonal directions, which agree with previous reports<sup>40,41</sup>. A magnified HR-TEM image (Fig. 2e) taken from the STC surface with the FFT pattern of the CoO

particle shows that the ex-solved particle at the surface of STC has a face-centered cubic (FCC) structure<sup>42</sup>, and is socketed in the STC layer. We note that the particle was a pure Co one when it was formed during reductive heating in a vacuum chamber<sup>36</sup>. An energy dispersive X-ray spectroscopy (EDS) line scan following the arrow in Fig. 2c identifies a significant ex-solution of Co atoms to the surface of the STC layer within ~5 nm from the surface; this observation indicates that Co ex-solution is sensitive to the atoms at surface, which have higher free energy than do atoms in the bulk. (Fig. 2f)

The surface composition of strain-controlled STC thin films was measured by angle resolved X-ray photoelectron spectroscopy (AR-XPS) with a emission angles from 0° to 60° to quantify the relative Co enrichment with respect to the A-site cation (Sr) of each film (Fig. 3a). The sensitivity to surface composition increases as emission angle increases, so the fitting data of photoelectron spectra of each cation exhibit the relative compositional change of Co with the depth from the surface (Fig. S4). To eliminate technical difficulties in the XPS analysis, we used  $I_0$  (= [Co/Sr] at 0°) to refer to the ratio of the Co measured at a detection angle of 0° (sensitive to bulk composition) and  $I_\theta$  = ([Co/Sr] at  $\theta^\circ$ ) (increasingly surface-sensitive as  $\theta^\circ$  increases).  $I_\theta / I_0$  was then evaluated to represent the amount of Co ex-solution (Table S3).

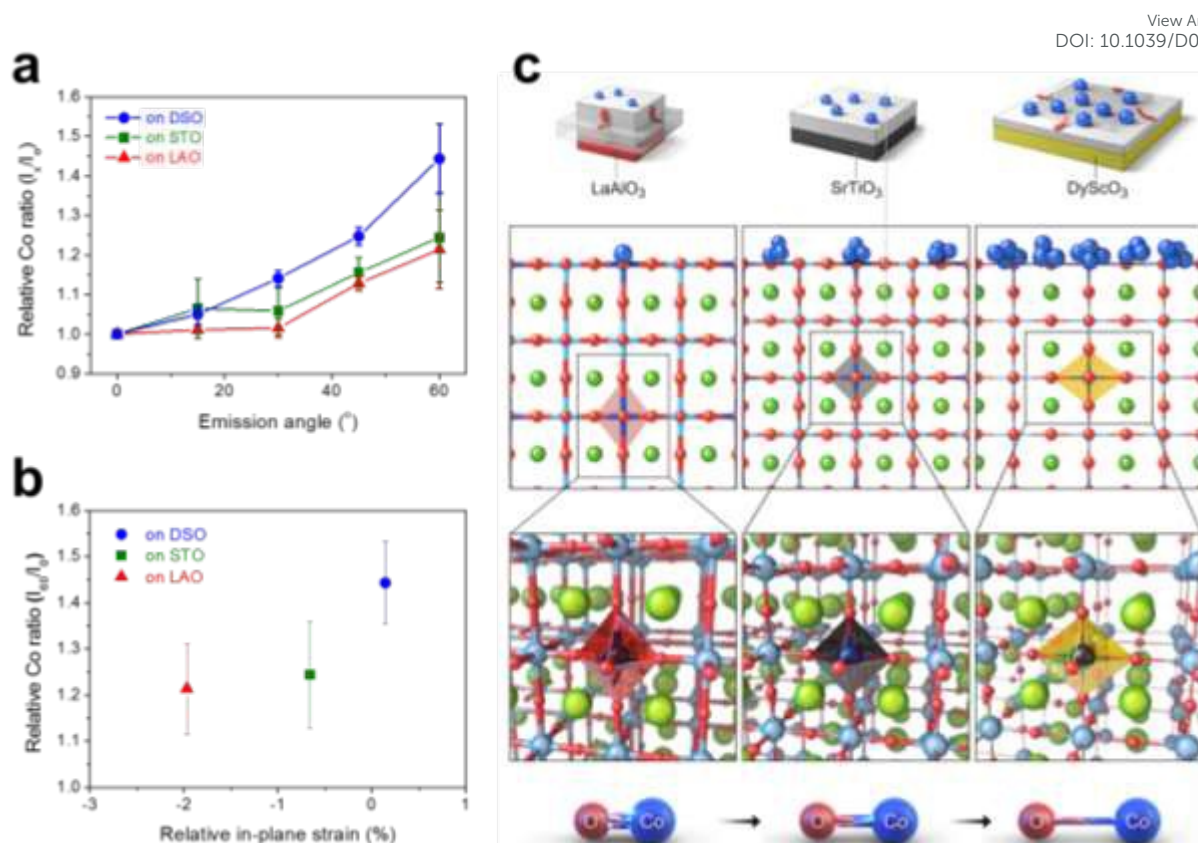


**Figure 3.** (a) Relative Co ratio of epitaxial  $\text{SrTi}_{0.75}\text{Co}_{0.25}\text{O}_{3-\delta}$  (STC) thin films on single-crystal  $\text{LaAlO}_3$  (LAO),  $\text{SrTiO}_3$  (STO) and  $\text{DyScO}_3$  (DSO) substrates measured by angle resolved X-ray photoelectron spectroscopy according to the emission angle. (b) Relative Co enrichment of epitaxial STC thin films vs. degree of induced in-plane strain. (c) Schematic illustration of how the strain changes Co-O bond length to control Co ex-solution.

All  $I_{\text{O}}/I_{\text{O}}$  increased continuously with increasing emission angle under lattice strain (Fig. 3b). In-plane stretched film on DSO shows significantly greater  $\text{Co}^{2+}$ -excess at the surface compared to the compressed STC films (Fig. S5); this result is in good agreement with our computational observation for the degree of Co ex-solution tendency in STC under different strain states. As a result, the weakening Co-O bond strength under tensile strain in the in-plane direction considerably accelerates the Co excess and promotes Co ex-solution at the STC surface; i.e., the Co ex-solution that depends on the Co-O bond strength (biaxial strain in experiment) is a response to the instability of cations in the perovskite lattice. Charge density distributions near Co-O bonds also clearly show that tensile strain weakens the Co-O bond

strength and facilitates Co ex-solution, whereas compressive strain strengthens these bonds and impedes Co ex-solution (Fig. 3c and S6). In mild reducing conditions, Ti is expected to maintain its oxidation state and position, unlike Co. To confirm this, additional AR-XPS analysis was performed. Unlike the increase in Co composition at the surface of the STC epitaxial thin film according to the in-plane deformation, the composition of Ti remains almost constant (Fig. S7). It was recently reported that the degree of Ni ex-solution can be changed by applying strain to  $\text{La}_{0.2}\text{Sr}_{0.7}\text{Ni}_{0.1}\text{Ti}_{0.9}\text{O}_{3-\delta}$  (LSNT) thin films<sup>43</sup>, possibly because misfit-strain relaxation energy changes the nature of Ni exsolution. Our findings here suggest that the misfit-strain energy in LSNT might be caused by change in Ni-O bond strength under different strain states.

In a technical aspect, however, applying the external strain to STC by lattice mismatch between thin film and substrate is not practical under reaction condition of the catalyst. Rather, engineering of size mismatch between host and dopant elements by isovalent doping is a simple and more effective way to control the Co-O bond strength. In this case, the isovalent element doped into the bulk perovskite of STC induces isostatic strain, not biaxial strain. DFT calculations demonstrated that the Co-O bond length steadily increased as the isostatic tensile strain was applied (Fig. 4a). The responses of  $E_{\text{X,vac}}$  upon the applied isostatic strain were similar to those observed under biaxial strain in bulk STC (Fig. 4b). This similarity implies that isostatic tensile strain can also be used to boost Co ex-solution by weakening the Co-O bond strength.



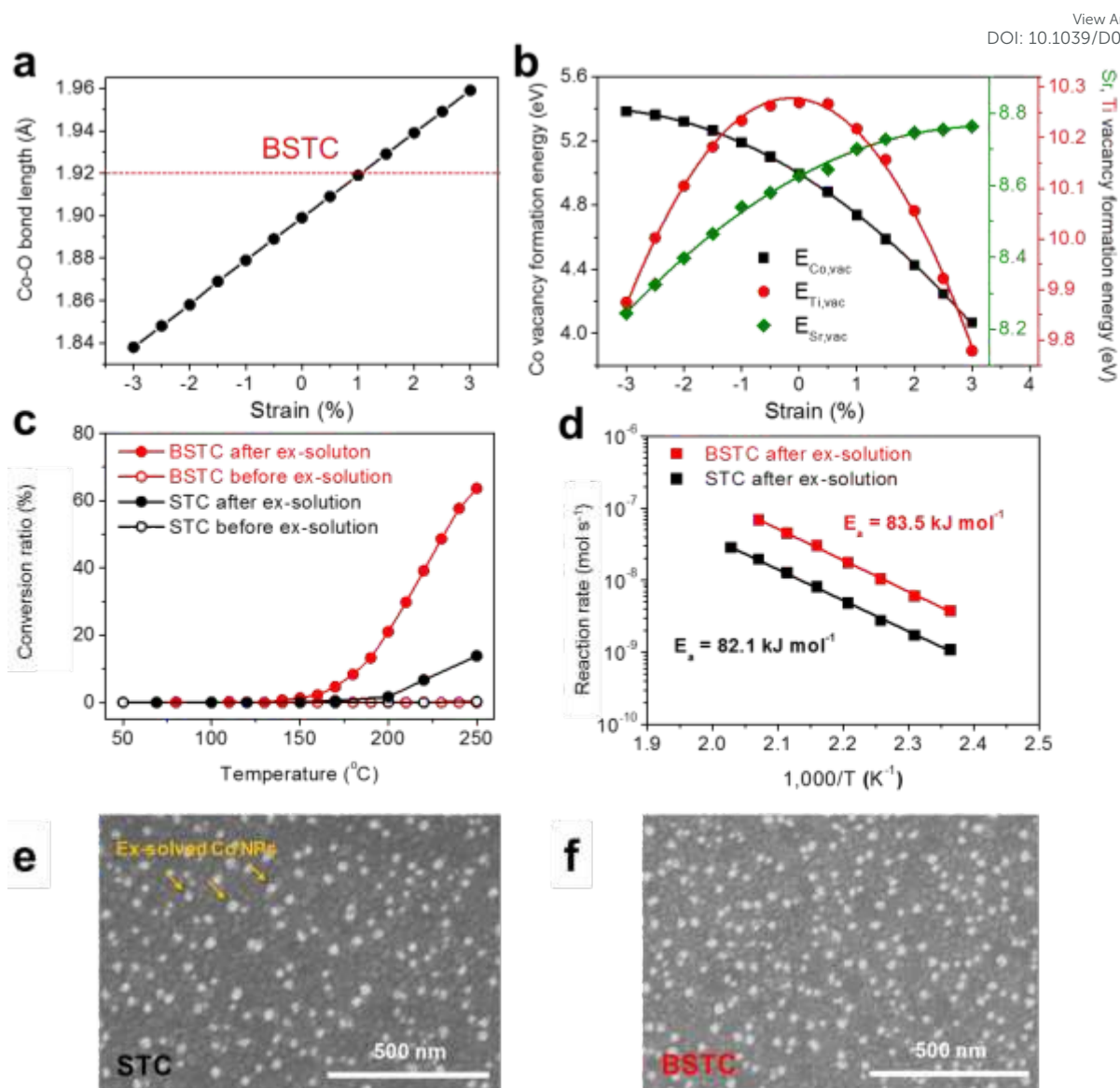


**Figure 4.** (a) DFT-calculated Co-O bond length and (b) Co, Sr, and Ti vacancy formation energies ( $E_{\text{Co,vac}}$ ,  $E_{\text{Sr,vac}}$ ,  $E_{\text{Ti,vac}}$ ) in bulk STC as a function of isostatic strain. A red dotted line is the Co-O bond length in BSTC. (c) Catalytic activity curves for CO conversion ratio with respect to temperature of polycrystalline STC thin films with or without 5 at.% Ba doping. (d) Arrhenius-type plots for CO oxidation of polycrystalline STC thin film with or without 5 at.% Ba doping. (e) Surface morphology of polycrystalline STC thin films after catalytic activity test of CO oxidation by scanning electron microscopy (SEM) techniques and (f) with 5 at.% Ba doping.

Isovalent doping induces isostatic strain in all  $x$ ,  $y$ , and  $z$  directions because size mismatch between the dopant and host affects all surrounding atoms in the perovskite structure, and

thereby affects both in-plane and out-of-plane lattice parameters. In contrast, biaxial tensile strain causes decrease in the out-of-plane lattice parameter and increase in in-plane lattice parameters. Therefore, more strain is applied by isostatic strain than by biaxial strain under the same degree of applied strain, so the slope of  $E_{\text{X,vac}}$  for isostatic strain was steeper (Fig. 4b) than that for biaxial strain (Fig. 1c).

To enlarge the Co-O bond by isovalent doping, we doped 5 at% Ba into the Sr site in our STC model, because Ba has the same charge state of 2+ but a larger ionic radius of 1.61 Å than the host  $\text{Sr}^{2+}$  (1.44 Å) when the coordination number is 12. As expected, Ba induced a significant increase of Co-O bond length to 1.92 Å in Ba-doped STC (BSTC) without any external strain (Fig. 4a, S8, and Table S4). This elongation corresponds locally to the isostatic strain of 1.03%. Doping with Ba weakened the Co-O bond strength, so the Co vacancy formation energy  $E_{\text{Co,vac}}$  was decreased from 4.93 eV in STC to 4.73 eV in BSTC (Table S5).

To demonstrate that isovalent doping can promote Co ex-solution, we experimentally observed how the Co NPs formed on the surface of STC polycrystalline films differ depending on the presence of Ba dopants, and also evaluated their catalytic properties using a fixed-bed flow microreactor combined with a quadrupole mass spectrometers (QMS). XRD (Fig. S9) showed that 5 at.% Ba doping expanded the lattice constant of STC materials with increase of the Co-O bond length in the lattice by approximately 0.4 % (Table S6). Compositional analysis by X-ray fluorescence (XRF) measurement confirmed that the STC and BSTC films were well-fabricated (Table S7). Co particles of similar size, whether Ba doped or not, are uniformly produced on the STC surface, but more particles are observed in the Ba-doped sample (Fig. S10). To investigate the effect of Ba doping ratio to enlarge (weaken) the Co-O bond length (strength), we synthesized STC powders and carried out their XRD analyses, varying the Ba concentration to 5, 10, 20 at%. As a result, the Co-O bond length gradually increased according to the Ba doping concentration (Fig. S11 and Table S8).



These observations evidently support that Ba doping can promote Co ex-solution (Table S9).

Light-off curves for CO oxidation (Fig. 4c) show that Co/BSTC had four times higher catalytic activity to convert CO to CO<sub>2</sub> than Co/STC sample, whereas samples without Co ex-solution give no conversion of CO regardless of the presence of Ba in the STC support. However, similar activation energies were observed for both ex-solved samples regardless of the Ba doping, indicating that CO oxidation occurred through the similar reaction pathway (Fig. 4d and S12). We also investigated the surface morphology and chemical composition of the samples by using SEM and AR-XPS analysis (Fig. 4e, f, and S13). Ex-solved Co NPs were larger on the surface of BSTC films (Fig. 4f) than on the surface of STC sample without Ba doping (Fig. 4e). The relationship between relative Co intensity and emission angle further confirmed the Co enrichment on the surface of BSTC films (Fig. S13).

To summarize, when Ba cation is doped into the A-site of STC perovskite, the amount of ex-solved Co increases, and catalytic activity for CO oxidation increases. Irvine *et al.* previously observed uniformly dispersed Ni NPs on La<sub>0.52</sub>Sr<sub>0.28</sub>Ni<sub>0.06</sub>Ti<sub>0.94</sub>O<sub>3-δ</sub> after reduction at 930 °C for 20 h in 5% H<sub>2</sub>/Ar<sup>15</sup>. They explained that A-site deficiency in the perovskite oxide destabilized the perovskite structure, so the B-site cation was spontaneously ex-solved during high-temperature reduction. We believe that the B-O bond strength could be influenced by the deficiency of A-site at the atomic level. Thus, A-site deficiency might have a similar effect as isovalent doping in this study in accelerating B-site ex-solution.

## Conclusion

This study investigated the influence of Co-O bond strength change on the Co ex-solution in SrTi<sub>0.75</sub>Co<sub>0.25</sub>O<sub>3-δ</sub> (STC) surface. The weakened Co-O bond strength upon the tensile strain, promotes surface Co ex-solution significantly. This observation suggests that doping a large isovalent element to extend the Co-O bond length is a new strategy to improve the catalytic

activity of perovskite-type oxides for CO oxidation. This doping is an effective method to promote ex-solution and can be readily applied to various heterogeneous catalysts.

## Methods

### *Sample preparation*

SrTi<sub>0.75</sub>Co<sub>0.25</sub>O<sub>3-δ</sub> (STC) thin films were grown onto (001)-oriented LaAlO<sub>3</sub> (LAO), SrTiO<sub>3</sub> (STO) and (110)-oriented DyScO<sub>3</sub> (DSO) single-crystal substrates (10 mm × 10 mm × 5 mm, Crystec) by pulsed laser deposition (PLD) from an oxide target. STC was prepared by a conventional solid state method, starting with SrCO<sub>3</sub> (Sigma Aldrich, 99.99%), TiO<sub>2</sub> (Sigma Aldrich, 99.8%), and Co<sub>3</sub>O<sub>4</sub> (Alfa Aesar, 99.7%) powders. The powders were mixed to obtain the desired Sr:Ti:Co stoichiometric ratios (1.00:0.75:0.25), then ball milled with high-purity ethanol (Merck, 99.9%) for 24 h before drying. The well-mixed powders were then calcined in air at 1200 °C for 8 h with heating and cooling rates of 4 °C/min. A pellet-type STC target for PLD was prepared by uniaxial pressing followed by cold isostatic pressing at 200 MPa. The resulting compacted green bodies were sintered at 1350 °C for 8 h with heating and cooling rates of 4 °C/min. STC doped with 5 at.% Ba (BSTC) was prepared in the same way, as STC but with added BaCO<sub>3</sub> (Sigma Aldrich, 99.98%).

The PLD system (VTS Corporation) was operated with a KrF excimer laser, emitting at 248 nm (Coherent COMPex Pro 205), with an energy of 280 mJ/pulse with a repetition rate of 2 Hz for 5 min. The substrates were heated to 700 °C during deposition, while the oxygen pressure was maintained at 10 mTorr after pumping the background pressure to 10<sup>-5</sup> Torr. After deposition, the oxygen pressure in the chamber was decreased to < 10<sup>-5</sup> Torr at 700 °C for 1 h to induce relatively high-temperature reduction. The resulting films had a typical thickness of ~25 nm. Polycrystalline STC and BSTC thin films were grown by PLD from the

same targets and deposited onto 2-inch Si wafer with the same heating profile that was used to fabricate epitaxial STC thin films with a repetition rate of 10 Hz for 30 min.

### *Physical and chemical characterization*

High-resolution thin film XRD (HR-XRD, X'Pert-PRO MRD, PANalytical) measurements were performed for both the in-plane and out-of-plane alignments of STC thin films on single-crystal LAO(001), STO(001), and DSO(110) substrates using Cu K $\alpha$  radiation ( $\lambda = 1.541 \text{ \AA}$ ). The HR-XRD was operated at 45 kV and 40 mA with a hybrid monochromator including a four-bounce Ge(220) crystal and a parabolic multilayer mirror.  $2\theta$ - $\omega$  scan (out-of-plane) in range of  $20^\circ$  to  $60^\circ$  and  $\phi$  scan (in-plane) were performed to investigate the crystallographic orientation and strain state of thin films. The in-plane reflection of thin films was measured from the (110) plane parallel with the substrate by  $45^\circ$  as the (111) plane of a cubic structure.

Structural and compositional analyses of the STC thin film and single-crystal DSO substrate were performed using a high-resolution transmission electron microscope (HR-TEM, Tecnai G2 F30, FEI company) equipped with an energy dispersive X-ray spectroscope (EDS). The TEM sample was prepared by focused ion beam (FIB, Quanta 3D FEG, FEI company) milling. Angle-resolved X-ray photoelectron spectroscopy (AR-XPS, K-alpha, Thermo VG Scientific) of the surface of thin films was performed using a rotating sample-stage in angle-resolved mode ( $0^\circ$ ,  $15^\circ$ ,  $30^\circ$ ,  $45^\circ$ , and  $60^\circ$ ) under ultrahigh vacuum ( $\sim 10^{-9}$  Torr) using monochromated Al K $\alpha$  ( $h\nu = 1486.6 \text{ eV}$ ) radiation. All AR-XPS spectra were energy calibrated to the C-C peak ( $284.8 \text{ eV}$ ) in the C 1s spectrum by using the Shirley background.

### Computational details

Density functional theory (DFT) calculations were performed using the Vienna *ab initio* Simulation Package<sup>44</sup>. The Perdew-Burke-Ernzerhof functional based on the generalized gradient approximation (GGA) was used, with the plane-wave expansion up to a cutoff energy of 400 eV<sup>45</sup>. The DFT+U approach was considered with  $U_{\text{eff}} = 4.4$  eV for Ti and  $U_{\text{eff}} = 3.4$  eV for Co to correct the self-interaction errors<sup>46</sup>. The bulk STC was constructed by replacing a Ti atom with a Co atom in the  $(2 \times 2 \times 2)$  supercell of STO. To investigate the change in the energetics of bulk STC upon the applied strain, only the  $z$ -direction of bulk STC structures was relaxed with the fixed strained lattice parameters in the  $x$ - and  $y$ -directions (in-plane)<sup>35</sup>. For the isostatic strain, we relaxed bulk structures with the strained lattice parameters in all of the  $x$ ,  $y$ , and  $z$  directions. Monkhorst-Pack grids of  $6 \times 6 \times 6$  and  $4 \times 4 \times 1$   $k$ -points<sup>47</sup> were used for bulk and slab models of STC, respectively.

To understand the ex-solution phenomenon of Co atoms in STC, we calculated  $E_{\text{Co,seg}}$  using an asymmetric CoO-terminated STC slab model by cleaving the bulk STC (Fig. S1a) along the (001) plane (Fig. S1b) as experimentally observed. An eight-layered slab with a vacuum thickness of  $\sim 14$  Å was used. The segregation energy was calculated by the total energy difference between Co located at surface and in bulk (Fig. S1b). The Sr, Ti, and Co vacancy formation energies under biaxial strain were calculated by the total energy difference with/without an A- or B- defect in STC as<sup>35</sup>

$$E_{X,vac}(eV) = (E_{STC,bulk}^{X,vac} + E_X) - E_{STC,bulk}^{bare},$$

where  $E_{STC,bulk}^{X,vac}$  is the total energy of bulk STC with a cation vacancy, and  $E_{STC,bulk}^{bare}$  is the total energy of defect-free STC.  $E_X$  is the chemical potential of cation. The chemical potentials  $E_{\text{Co}}$ ,  $E_{\text{Ti}}$  and  $E_{\text{Sr}}$  were calculated from their bulk phases.

### Catalytic activity test

Catalytic activity tests of carbon monoxide (CO) oxidation were conducted at atmospheric pressure in a fixed-bed flow quartz reactor that had an internal diameter of 1/4 inch. To build a catalytic bed, the amount of cleaved STC thin films from three 2-inch wafers was loaded between layers of quartz wool. The temperature of the sample was measured using a K-type thermocouple which was in contact with the catalytic bed. Before the test, the bed was annealed to remove surface adsorbents or contaminants. The reactant gas mixture was 1 vol.% CO, 4 vol.% O<sub>2</sub>, and 95 vol.% Ar, and was fed at 50 mL min<sup>-1</sup>. The reactant and product gases were monitored using a quadrupole mass spectrometer (MS, GSD320, Pfeiffer Vacuum) in real time.

### Acknowledgments

This study was supported by the Samsung Research Funding Center for Future Technology (SRFC-MA1502-52).

### Author contributions

K.K., B.K., W.J., and J.W.H. designed the experiments. K.K. performed DFT calculations and analyzed theoretical results. B.K. and J.K.K. prepared and characterized all of the thin-film samples. S.L. examined catalytic activity. Y-R.J. and B-J.K. performed TEM analysis. All of the authors contributed to writing the manuscript. B-J.K., W.J., and J.W.H. supervised and guided the entire project.

### Competing interests

The authors declare no competing interests.

### References

- 1 D. Astruc, F. Lu and J. R. Aranzaes, *Angew. Chem. Int. Ed.*, 2005, **44**, 7852-7872.
- 2 J. M. Campelo, D. Luna, R. Luque, J. M. Marinas and A. A. Romero, *ChemSusChem*, 2009, **2**, 18-45.

- 3 W. C. Chueh, Y. Hao, W. Jung and S. M. Haile, *Nat. Mater.*, 2012, **11**, 155-161.
- 4 W. Jung, K. L. Gu, Y. Choi and S. M. Haile, *Energy & Environ. Sci.*, 2014, **7**, 1685-1692.
- 5 Y. Wang, T. Liu, M. Li, C. Xia, B. Zhou and F. Chen, *J. Mater. Chem. A*, 2016, **4**, 14163-14169.
- 6 A. A. Herzing, C. J. Kiely, A. F. Carley, P. Landon and G. J. Hutchings, *Science*, 2008, **321**, 1331-1335.
- 7 D. K. Liguras, D. I. Kondarides and X. E. Verykios, *Appl. Catal. B-Environ.*, 2003, **43**, 345-354.
- 8 Y. Choi, S. K. Cha, H. Ha, S. Lee, H. K. Seo, J. Y. Lee, H. Y. Kim, S. O. Kim and W. Jung, *Nat. Nanotech.*, 2019, **14**, 245-251.
- 9 C. H. Bartholomew, *Appl. Catal. A-Gen.*, 2001, **212**, 17-60.
- 10 D. L. Trimm, *Appl. Catal. A-Gen.*, 2001, **212**, 153-160.
- 11 A. Cao, R. Lu and G. Veser, *Phys. Chem. Chem. Phys.*, 2010, **12**, 13499-13510.
- 12 C. G. Granqvist and R. A. Buhrman, *J. Catal.*, 1976, **42**, 477-479.
- 13 J. Seo, N. Tsvetkov, S. J. Jeong, Y. Yoo, S. Ji, J. H. Kim, J. K. Kang and W. Jung, *ACS Appl. Mater. Interfaces*, 2020, **12**, 4405-4413.
- 14 S. Lee, J. Seo and W. Jung, *Nanoscale*, 2016, **8**, 10219-10228.
- 15 D. Neagu, G. Tsekouras, D. N. Miller, H. Ménard and J. T. S. Irvine, *Nat. Chem.*, 2013, **5**, 916.
- 16 O. Kwon, S. Sengodan, K. Kim, G. Kim, H. Y. Jeong, J. Shin, Y.-W. Ju, J. W. Han and G. Kim, *Nat. Commun.*, 2017, **8**, 15967.
- 17 G. Yang, W. Zhou, M. Liu and Z. Shao, *ACS Appl. Mater. Interfaces*, 2016, **8**, 35308-35314.
- 18 M. van den Bossche and S. McIntosh, *Chem. Mater.*, 2010, **22**, 5856-5865.
- 19 D. Neagu, T.-S. Oh, D. N. Miller, H. Ménard, S. M. Bukhari, S. R. Gamble, R. J. Gorte, J. M. Vohs and J. T. S. Irvine, *Nat. commun.*, 2015, **6**, 8120.
- 20 S. Liu, Q. Liu and J.-L. Luo, *ACS Catal.*, 2016, **6**, 6219-6228.
- 21 Y.-F. Sun, Y.-Q. Zhang, J. Chen, J.-H. Li, Y.-T. Zhu, Y.-M. Zeng, B. S. Amirkhiz, J. Li, B. Hua and J.-L. Luo, *Nano Lett.*, 2016, **16**, 5303-5309.
- 22 Y. Gao, J. Wang, Y.-Q. Lyu, K. Lam and F. Ciucci, *J. Mater. Chem. A*, 2017, **5**, 6399-6404.
- 23 J.-h. Myung, D. Neagu, D. N. Miller and J. T. S. Irvine, *Nature*, 2016, **537**, 528.

- 24 J. T. S. Irvine, D. Neagu, M. C. Verbraeken, C. Chatzichristodoulou, C. Graves and M. B. Mogensen, *Nat. Energy*, 2016, **1**, 15014.
- 25 Y. Li, W. Zhang, Y. Zheng, J. Chen, B. Yu, Y. Chen and M. Liu, *Chem. Soc. Rev.*, 2017, **46**, 6345-6378.
- 26 J. H. Kim, J. K. Kim, H. G. Seo, D.-K. Lim, S. J. Jeong, J. Seo, J. Kim and W. Jung, *Adv. Funct. Mater.*, 2020, 201326.
- 27 N. W. Kwak, S. J. Jeong, H. G. Seo, S. Lee, Y. Kim, J. K. Kim, P. Byeon, S.-Y. Chung and W. Jung, *Nat. Commun.*, 2018, **9**, 4829.
- 28 S. Li, Q. Qin, K. Xie, Y. Wang and Y. Wu, *J. Mater. Chem. A*, 2013, **1**, 8984-8993.
- 29 M. B. Katz, S. Zhang, Y. Duan, H. Wang, M. Fang, K. Zhang, B. Li, G. W. Graham and X. Pan, *J. Catal.*, 2012, **293**, 145-148.
- 30 Y. Gao, D. Chen, M. Saccoccio, Z. Lu and F. Ciucci, *Nano Energy*, 2016, **27**, 499-508.
- 31 T.-S. Oh, E. K. Rahani, D. Neagu, J. T. S. Irvine, V. B. Shenoy, R. J. Gorte and J. M. Vohs, *J. Phys. Chem. Lett.*, 2015, **6**, 5106-5110.
- 32 O. Kwon, K. Kim, S. Joo, H. Y. Jeong, J. Shin, J. W. Han, S. Sengodan and G. Kim, *J. Mater. Chem. A*, 2018, **6**, 15947-15953.
- 33 J. K. Kim, Y.-R. Jo, S. Kim, B. Koo, J. H. Kim, B.-J. Kim and W. Jung, *ACS Appl. Mater. Interfaces*, 2020, **12**, 24039-24047.
- 34 B. Koo, K. Kim, J. K. Kim, H. Kwon, J. W. Han and W. Jung, *Joule*, 2018, **2**, 1476-1499.
- 35 B. Koo, H. Kwon, Y. Kim, H. G. Seo, J. W. Han and W. Jung, *Energy & Environ. Sci.*, 2018, **11**, 71-77.
- 36 Y.-R. Jo, B. Koo, M.-J. Seo, J. K. Kim, S. Lee, K. Kim, J. W. Han, W. Jung and B.-J. Kim, *J. Am. Chem. Soc.*, 2019, **141**, 6690-6697.
- 37 T. Mayeshiba and D. Morgan, *Solid State Ion.*, 2017, **311**, 105-117.
- 38 G. J. la O', S.-J. Ahn, E. Crumlin, Y. Orikasa, M. D. Biegalski, H. M. Christen and Y. Shao-Horn, *Angew. Chem. Int. Ed.*, 2010, **49**, 5344-5347.
- 39 H. Ledbetter, M. Lei and S. Kim, *Phase Transitions*, 1990, **23**, 61-70.
- 40 JCPDS of perovskite structure SrTiO<sub>3</sub>: No. 35-0734.
- 41 JCPDS of orthorhombic structure DyScO<sub>3</sub>: No. 27-0204.
- 42 JCPDS of face-centered cubic structure CoO: No. 78-0431.
- 43 H. Han, J. Park, S. Y. Nam, K. J. Kim, G. M. Choi, S. S. P. Parkin, H. M. Jang and J. T. S. Irvine, *Nat. commun.*, 2019, **10**, 1471.

- 44 G. Kresse and J. Furthmüller, *Phys. Rev. B*, 1996, **54**, 11169-11186.
- 45 J. P. Perdew, K. Burke and M. Ernzerhof, *Phys. Rev. Lett.*, 1996, **77**, 3865-3868.
- 46 L. Wang, T. Maxisch and G. Ceder, *Phys. Rev. B.*, 2006, **73**, 195107.
- 47 Monkhorst, H. J. and Pack, J. D. Special points for Brillouin-zone integrations. *Phys. Rev. B.* **13**, 5188-5192 (1976).